https://doi.org/10.1016/j.ijrmms.2023.105360

Experimental validation of a velocity discontinuity model for prediction of the seismic and static shear stiffness of rock joints

Hua Li[1], Amin Gheibi[2], Ahmadreza Hedayat[3], Jianhua Yin[4], Jianhui Deng[1*]

[1] College of Water Resource and Hydropower, Sichuan University, Chengdu, China

[2] Design and Consulting Services, AECOM, Denver, CO, USA

[3] Department of Civil and Environmental Engineering, Colorado School of Mines, Golden, CO, USA

[4] Department of Civil and Environmental Engineering, The Hong Kong Polytechnic University, Hong Kong, China

* Corresponding author; Email: jhdeng@scu.edu.cn

Abstract: The stiffness estimation of rough joint is of great significance in rock engineering problems. In general, the value of stiffness measured by seismic wave propagation gives the upper boundary value, while the stiffness determined by static measurements provides the lower boundary value. Several experimental studies on mated fractures quantified this difference in stiffness and revealed that seismic stiffness is two to eight times larger than static stiffness. However, the underlying physical mechanisms responsible for this discrepancy are still poorly understood. In the study presented in this paper, the difference between seismic and static shear stiffnesses was attributed to the strain-level and rate effects. A velocity discontinuity model, composed of the Hooke, modified Saint Venant, and Newton elements, was developed and used for interpretation of experimentally collected shear waves transmitted through a rock joint. The small-strain stiffness defined by the model was relevant to the wave energy dissipation at high frequencies, providing an approximate value of joint seismic stiffness. The rate-independent stiffness of this model was associated with joint responses at low frequencies, providing an estimation of the static stiffness. Thus, the joint stiffness determined by this model is not a constant in the frequency domain. The stiffness value is smaller at low frequencies than at high frequencies, achieving a better prediction about the wave attenuation at a rough joint compared with a displacement discontinuity model. The developed joint model in this study enables estimation of both the seismic and static stiffnesses of rough joints by simple shear wave transmission experiments and thereby contributes some new understanding of strain rate effects.

Keywords: rock joint; shear stiffness; ultrasonic wave; viscoelastic; velocity discontinuity

1 Introduction

The design of rock slopes, foundations, and underground space is strongly dependent on deformation properties of rock masses. However, joints, as well as other recurrent discontinuities, change the mechanical, hydraulic, and geophysical properties of rock masses, causing difficulties in providing economical and reliable design in rock engineering[1-3]. To date, many experimental and theoretical studies have been done to estimate the value of joint stiffness, which is defined as the ratio of the stress increment to the displacement increment caused by the deformation of the void space between joint surfaces[4-7]. A detailed classification of joint stiffness according to strain rate ($\dot{\varepsilon}$) has been presented by Zhang &Zhao[7], who suggested that the static and dynamic stiffnesses determined by static ($\dot{\varepsilon} \leq 10^{-1}\ s^{-1}$) and dynamic ($10^{-1} \leq \dot{\varepsilon} \leq 10^{6}\ s^{-1}$) stress-displacement measurements are "large-deformation ($\varepsilon \geq 0.1\%$)" stiffnesses, while the seismic stiffness determined by ultrasonic wave propagation ($\dot{\varepsilon} \geq 10^{6}\ s^{-1}$) is "small-strain($\varepsilon \leq 0.0001\%$)" stiffness or, more precisely, the stiffness at "very small strain."

Similar to the small-strain modulus of granular materials, the seismic stiffness of joints is relatively greater than the dynamic stiffness[8-11], and the dynamic stiffness of joints is typically larger than the static stiffness, called "stiffness hardening"[12-15]. Cai[16] quantified the difference and demonstrated that the dynamic shear stiffness of mated rock joints was approximately 1.2 to 2 times as high as the static stiffness, and that seismic stiffness was 2 to 3 times larger than dynamic stiffness. The higher value of seismic stiffness is related to the following three aspects: first, seismic stiffness is determined by the wave-induced dynamic load, which is much smaller than the static load applied in practice[17, 18]; second, seismic stiffness is obtained at the very small strain level, where deformation seems to be linear and recoverable[19-22]; third, seismic stiffness is determined at high strain rates, where joint asperities may not have enough time to deform, causing localized strain hardening on joint surfaces[19, 23, 24]. Therefore, seismic stiffness and static stiffness are two special cases of dynamic stiffness. The former is characterized by small strain levels and high strain rates. The latter displays low-strain-rate properties.

Theoretically speaking, the difference between the static and seismic stiffnesses of joints relies largely on the joint mechanical model used in wave propagation. Usually, seismic shear stiffness is determined on the basis of the displacement discontinuity model (DDM)[25-27], where the joint is simplified as a spring with a constant stiffness. With this model, the predicted and measured spectra of the transmitted/reflected waves are compared in order to acquire an estimation of the

average joint stiffness in the frequency domain. A detailed introduction of this approach was given by Pyrak-Nolte *et al.*[25]. Although general agreement can be achieved between the predicted and measured spectral amplitudes by assuming the DDM, minor discrepancies still exist at low frequencies, where the predicted spectral amplitudes are consistently larger than the measured ones[16]. Other models, such as the Kelvin model and the Maxwell model, are velocity/rate-dependent models, which also have been successfully applied to wave propagation to obtain a full solution for the reflection and transmission coefficients[23, 28, 29]. However, the application of these models is limited as the joint stiffness calculated by these models is not a constant in the frequency domain[30]. Although many studies have pointed out that the stiffness of rough joints is frequency-dependent in nature[19, 31, 32], limited studies have attempted to interpret this feature theoretically and associate it with the difference between the static and seismic stiffnesses of joints.

Although extensive studies have been conducted to investigate the slip process of joints from initiation to rupture, measuring joint shear stiffness during shearing is still challenging[33]. Shear resistance along a joint cannot be uniform due to the existence of zones with different shear properties[34, 35]. Slip distributions also are non-uniform and cannot occur simultaneously on the joint surfaces[36-38]. Therefore, ignoring the non-uniform slipping process is not appropriate for measuring the static and seismic shear stiffnesses of joints. Recently, digital image correlation (DIC) and the seismic monitoring method have been widely accepted and successfully used to investigate the local physical and mechanical properties of joints. DIC, a full-field deformation measurement technique, directly captures the surface deformation of joints by comparing the digital images taken before and after deformation[39-41]. The seismic monitoring method, in particular compressional and shear wave propagation, uses a set of electronically activated transducers to transmit ultrasonic waves through joints and probes the local contacts on joint surfaces[25, 42, 43].

In this study, the difference between the seismic and static shear stiffnesses of joints was attributed to the strain-level and rate effects. A velocity discontinuity model composed of Hooke, modified Saint Venant, and Newton elements, was developed in this study to estimate the values of both the seismic and static stiffnesses of rough joints by simple shear wave transmission experiments. Model validation was conducted by comparing model predictions with laboratory measurements obtained by seismic wave transmission and DIC technique.

2 The Hooke-modified Saint Venant/Newton (HSVN) model

The HSVN model, as shown in Fig. 1, was originally proposed to describe the dynamic hardening behavior of rough joints[44, 45]. The Hooke element is introduced to reflect the elastic/recoverable deformation; the Newton element is used to produce the rate-related stress component under dynamic conditions; and the modified Saint Venant element is introduced to incorporate the irreversible hardening process. Noteworthy, the traditional Saint Venant is a perfect plastic model with a fixed yield limit, which is determined by the pre-compressed springs between two parallel frictional surfaces, as shown in Fig. 2a. In contrast, the modified Saint Venant element is a nonlinear plastic model (Fig. 2b), in which the two springs are placed between two inclining frictional surfaces to produce an alterable yield limit. Like the compressive hardening behavior, the shear hardening/yielding of rough joints is also the macro consequence of the opening of microcracks[7, 44, 46]; thus, there is every reason to use similar conceptual models to describe the rate-dependent behavior of joints in both compression and shear.

The HSVN model is a typical excess stress model. When the strain rate is constant at a very low level, the rate-dependent effects represented by the Newton element become negligible (viscosity coefficient tends to zero). The HSVN model "degrades" into the Hooke-modified Saint Venant (HSV) model (see Fig. 3), describing a rate-independent or static deformation process. When the strain value lies within a minimum range, the stiffness of the Hooke element (k_0), can be a constant and is equivalent to "very small strain" stiffness, which is the micro consequence of the dynamic response of a solid material subjected to seismic excitations in the bender element test[19]. Similarly, high-frequency components in ultrasonic testing only produce a small-strain response. The HSVN model "degrades" into a Hooke model due to the existence of the dashpot (viscosity coefficient tends to infinity). This is the reason why ultrasonic testing is usually regarded as a nondestructive measurement of the solid-solid contact condition[11].

Thus, in wave propagation, the small-strain stiffness given by the Hooke element and the rate-independent stiffness given by the HSV model determine the upper and lower boundary values of the joint stiffness, respectively. In theory, the small-strain stiffness should be sensitive to the wave energy dissipation at high frequencies, while the rate-independent stiffness is sensitive to the attenuation of the low-frequency portions in the frequency domain. Thus, wave energy dissipation at high and low frequencies can be studied separately by the developed joint model. The rate-

independent stiffness is a reasonable prediction of joint static stiffness, and the small-strain stiffness predicts the joint seismic stiffness.

A normally incident shear (S-) wave impinging on a discontinuity represented by the HSVN model has the following boundary conditions:

$$\sigma_H = k_0 A e^{-i\omega t} \tag{1}$$

$$\sigma_N = \eta \frac{dBe^{-i\omega t}}{dt} = -i\eta\omega B e^{-i\omega t} \tag{2}$$

$$\sigma_{M\_S} = 2k_1 \tan\theta \tan(\varphi + \theta) B e^{-i\omega t} = k_1' B e^{-i\omega t} \tag{3}$$

where subscripts *H*, *N*, and *M_S* represent the Hooke, Newton, and modified Saint Venant elements, respectively; k_0 is the stiffness of the Hooke element; η is the specific viscosity of the Newton element; k_1' denotes the effective stiffness in the modified Saint Venant element; *A* and *B* are amplitudes; ω is angular frequency; and *t* represents time.

The global stiffness of the HSVN model is:

$$k = \frac{k_0 k_1' - i k_0 \eta\omega}{k_0 + k_1' - i\eta\omega} \tag{4}$$

The transmission coefficient $T(\omega)$ for a shear wave propagated at normal incidence across an elastic discontinuity, i.e., assuming the DDM, has been derived by Pyrak-Nolte *et al.*[25]:

$$T(\omega) = \frac{1}{1 - i\omega Z/2k} \tag{5}$$

where *Z* is the seismic impedance as the product of phase velocity and density of the intact rock.

Thus, the transmission coefficient for a normally incident shear wave impinging on a HSVN contact is:

$$T(\omega)_{HSVN} = \frac{2k_0\sqrt{k_1'^2 + \eta^2\omega^2}}{\sqrt{\omega^2 Z^2 (k_1'^2 + \eta^2\omega^2) + k_0{}^2 \left[4k_1'^2 + \omega^2(2\eta + Z)^2\right] + 2k_0 k_1' \omega^2 Z^2}} \tag{6}$$

Eq. (6) defines the transmission coefficient over the entire frequency domain. For high-frequency components, the HSVN model "degrades" into the Hooke model, there is:

$$T(\omega)_H = \sqrt{\frac{4k_0{}^2}{4k_0{}^2 + \omega^2 Z^2}} \tag{7}$$

For low-frequency portions, the HSVN model "degrades" into HSV model, there is:

$$T(\omega)_{H-M\_S} = \sqrt{\frac{4\left(\frac{k_0 k_1'}{k_1' + k_0}\right)^2}{4\left(\frac{k_0 k_1'}{k_1' + k_0}\right)^2 + \omega^2 Z^2}} \tag{8}$$

Eqs. (7) and (8) are derived by assuming η in Eq. (6) tends to infinity and zero, respectively. If η is a positive constant, the values of the transmission coefficients determined by Eq. (6) should fall somewhere between the values determined by Eqs. (7) and (8), as shown in Fig. 4. Thus, there is a zone, in which the transmission-coefficient values or the predicted spectral amplitudes given by Eq. (6) are close to the values determined by Eq. (7). Also, in another frequency range, the values given by Eq. (6) are close to the values given by Eq. (8). The frequency domain is thus divided into three portions: high, medium/transition, and low-frequency, as shown in Fig. 4.

The value of η for a HSVN joint can be estimated by an analysis on wave attenuation at the residual strength stage, where the shear stress remains constant and the hardening and softening effects have completely vanished[31, 32]. Thus, the value of k_1' in the modified Saint Venant element decreases to zero. The HSVN model "degrades" into the Maxwell model, producing a constant driving force and a steady deformation rate. The transmission coefficient is thus determined by:

$$T(\omega)_{H-N} = \frac{2k_0\eta}{\sqrt{Z^2\eta^2\omega^2 + k_0{}^2(2\eta + Z)^2}} \tag{9}$$

When ω approaches to zero, $T(\omega)$ is a function of η and Z:

$$T(\omega \to 0)_{H-N} = \frac{1}{1 + \frac{Z}{2\eta}} \tag{10}$$

Since the seismic impedance (Z) is a pre-determined parameter, the value of η can be determined by Eq. (10). Then, the values of two other parameters of the HSVN model, i.e., k_1' and k_0, can be determined by the frequency analysis procedure introduced by Pyrak-Nolte *et al.*[25]. Experimentally observed spectra from intact rock specimens are multiplied by the transmission coefficient given by Eq. (6) to provide predicted spectra for the transmitted wave across a joint. The values of k_1' and k_0 are then determined by the best fitting between the predicted and the measured spectral amplitudes. More specifically, there are three steps: 1) pre-determining the value of k_0 based on the DDM, where the "best fit" is evaluated for the frequencies higher than

the dominant frequency; 2) pre-determining the value of k_1' using the HSVN model to give the "best fit" at the frequencies lower than the dominant frequency; and 3) adjusting the values of k_0 and k_1' slightly to reach the "best fit" in the whole effective frequency domain. As mentioned in Pyrak-Nolte *et al.*[25], the best-fit value can be determined by a linear regression of the plot of the predicted vs. the measured spectral amplitudes.

In fact, the transmission coefficient $T(\omega)$ for a HSVN discontinuity is a monotone increasing function with respect to both k_0 and k_1'. For a given value of k_0, there is only one k_1' value that is the "best fit" in the frequency domain, which means there is only one set of values of k_1' and k_0 that give the "best fit" between the measured and the predicted spectral amplitudes. k_0 represents the small-strain stiffness, and $k_0 k_1' / (k_1' + k_0)$ represents the rate-dependent stiffness.

3 Laboratorial determination of the seismic and static shear stiffnesses

3.1 Experimental setup

More than ten direct shear tests of rough rock joints were conducted in this study to investigate the stiffness evolution approaching shear failure. Seismic wave transmission and DIC were employed to determine the seismic and static stiffnesses, respectively.

The shear experiments were conducted on tension-fractured sandstone joints, which were prepared based on the intact sandstone blocks collected from Yunnan, China. The intact rock blocks were pre-cut with dimensions of 102 mm in length, 102 mm in width, and 54 mm in thickness and were fractured using the Brazilian technique to obtain the fully mated rough surfaces[47]. Four narrow grooves, with the dimensions of 10 mm in depth and 1 mm in width, were made along the lateral surfaces to induce fracturing toward the geometric centre. Fig. 5 shows images of a grooved sandstone block, and the obtained rough joint surfaces. Table 1 is a summary of the relevant physical and mechanical properties of the sandstone material. The exterior surfaces of the specimens were ground parallel and flat to ensure uniform normal and shear loadings. All the specimens were oven-dried at 100 ℃ for 24 h to remove any residual moisture before the test. The roughness of the joints was measured using a 2D profilometer manufactured by Empire Level, Mukwonago, Wisconsin, as shown in Fig. 5c. The 2D joint profile containing the steepest slopes along the shearing direction were extracted to characterize the surface morphology. The root mean square of the first deviation (Z_2) of the profile was calculated to estimate the value of the joint roughness coefficient.

The direct shear tests were carried out under constant normal load conditions using an instrumented shear testing apparatus at the Colorado School of Mines, as shown in Fig. 6. This apparatus was instrumented with a set of ultrasonic transducers (2S, 4S, 5S, and 8S in Fig. 6) for monitoring wave energy attenuation across the joints[40, 41, 43, 48]. The shear testing part of the apparatus was composed of horizontal and vertical loading frames for applying normal and shearing stresses, respectively. The applied normal and shear stresses were monitored by two pressure transducers. The shear wave transducers (Panametrics V153) used in this study are broadband with a central frequency of 1 MHz. The source transducers remained stationary in the tests, while the receiver transducers moved as part of the loading platen with a constant shear rate. Note that for stress waves in rocks, the velocity is roughly 2000-5000 m/s and the wavelength ranges from 2 mm to 5 mm corresponding to the frequency of 1 MHz. Thus, the wavelength and the size of mineral grains in rocks are of the same order of magnitude. Heterogeneity effects in wave measurement should be considered. A square wave pulser (Panametrics 5077PR) was employed to generate ultrasonic wave pulses with an amplitude of 300 V at a repetition rate of 5 KHz. The coupling between the transducers and the joint specimens was achieved by using oven-baked honey, which was baked at 90°C for 90 min and then cooled to room temperature. A thin adhesive plastic film was placed on the external surfaces of the specimens to prevent the penetration of the honey.

To investigate the local shear displacement, the DIC technique was adopted to measure the in-plane displacement field on the outward-facing specimen surface. A charge-coupled device camera (2448 by 2048 square pixel) with 35 mm focal length (Model CF35HA-1) was mounted at a fixed distance from the specimen with the optical axis perpendicular to the front surface, which was pre-coated with a textured spray paint to produce a random pattern of speckles, as shown in Fig. 5b. In the 2D-DIC method, the reference image (un-deformed specimen) was divided into small square groups of pixels (subsets), which led to generation of a standard virtual grid on the reference image. A similar process was conducted on the images recorded at different levels of shear loads. Then, the gray scale values in the subsets of the deformed images were compared with the reference image to obtain a correlation criterion as a function of the vertical and horizontal displacement. The maximum value in the distribution of the correlation criterion was determined to evaluate the displacement for that specific subset. The same procedure was repeated for other generated subsets

to compute the displacement throughout the surface of the specimen[49, 50]. The spatial resolution determined by the setup of the imaging system was less than 100 μm/pixel in this study.

During the tests, shear wave signals in the transmission mode and joint images were recorded every 1 sec. The shear rate was applied at 1 μm/s through a standard displacement-controlled procedure introduced by Gheibi &Hedayat[48]. The same normal stresses were applied in all the tests at 9 MPa, which was about 15% of the uniaxial compressive strength of the sandstone material. The maximal amount of shear displacement imposed on the rock joints was less than 2 mm in order that the change in signal amplitudes attributable to the misalignment of the source and receiver transducers was limited to less than 4%[51]. Also, there was no detectable change in the velocity of transmitted waves. Thus, waveform correction was not necessary in the present study.

3.2 Data analysis

Fig. 7a shows the transmitted shear waveforms recorded during shearing. The coda wave interferometry technique was employed to determine the arrival time by comparing the transmitted signals to the reference signal collected at the beginning of shear[52]. A taper with a window size of 7.23 μs (the red line in Fig. 7a) was multiplied by the collected shear waveforms to compute the spectral content. The right taper should neither change the shape of the spectral amplitude of the wave nor influence the frequency content of the signal. This tapering technique is discussed in detail in Gheibi &Hedayat[48].

The seismic stiffness of the joints in the ultrasonic wave propagation was determined by assuming the DDM. Here, the joints were simplified as the linear-elastic contacts between two isotropic and homogeneous half-spaces. A physical analog of this assumption is two elastic half-spaces coupled by a set of vertically and horizontally placed springs[26]. As defined by Eq.7, the transmission coefficient for a joint represented by the DDM is a function of the joint stiffness, frequency, and seismic impedance. The seismic stiffness of the joint thus was determined by comparing the predicted and measured spectral amplitudes in a trial-and-error process. As mentioned in Introduction, the obtained stiffness value is representative of the average joint stiffness in the frequency domain. Fig. 7b shows the measured S-wave spectral amplitudes during shearing and the predicted amplitudes calculated by assuming the DDM.

Since the DIC provided the shear displacement field on the lateral surface of the specimens, the local shear displacements near the transducers were estimated directly. Fig. 8a shows an example

of the shear displacement contour measured by the DIC. Two vertical cross sections, 4 mm apart from each other, were selected to determine the relative shear displacement along the joint. Four horizontal lines, showing the projected center of the ultrasonic transducers, were drawn to determine the relative shear displacement near the transducers. Fig. 8b shows the displacement profiles along the four cross sections at the moment of shear failure for joint specimen J-0.11 (the joint specimens were labelled as "J-Z_2" in this study). Fig. 9 illustrates the applied shear stress and the measured relative shear displacement at the four cross sections as a function of time for joint specimen J-0.11. A uniform sampling spacing of 1.5 sec was adopted to determine the value of static stiffness, which was defined by the ratio of the stress increment to the local relative displacement increment.

4 Comparisons between model predictions and laboratory measurements

Fig. 10 compares the model predictions and laboratory measurements of the static and seismic shear stiffnesses for joint specimen J-0.11, which underwent a steady frictional slipping process under the normal stress of 9 MPa. The measured seismic values were determined by assuming the DDM, and the measured static values were calculated based on the DIC data. The predicted stiffness values, including both the seismic and the static, were determined by assuming the HSVN model. Fig. 10a shows the stiffness results for transducer 2S. For the seismic stiffness, after the initial contact development process (roughly from 0 to 150 sec), both the predicted and measured values increased as the shear load was applied to the specimen. The maxima occurred prior to the peak shear stress and were followed by a significant decrease as additional shear slip occurred. The precursory peaks observed in both the measured and predicted values were indicative of the impending shear failure of the joint. For the static stiffness, the predicted values showed an increasing trend that was similar to the seismic stiffness, but they decreased more dramatically after reaching the peak. This rapid decrease was due to the very small value of $k_1{}'$ obtained near the peak stress. The induced increasing difference between k_0 and $k_1{}'$ contributed to the quick reduction of the value of $k_0 k_1'/(k_0+k_1')$, producing a small estimation on the static stiffness. Similarly, the measured static stiffness decreased to a very small value near the peak-stress point after fluctuating around a long-run average. This decreasing process was relatively steady compared to the predicted values. The average value was regarded as the "overall static stiffness" of the joint.

Data for transducers 4S (Fig. 10b) and 5S (Fig. 10c) shows a number of similarities with the results from transducer 2S. Precursors were observed in both measured and predicted seismic stiffnesses. Static stiffnesses, both the predicted and the measured, decreased dramatically to a small value before the stress peaked. The measured values of seismic stiffness were around three to five times greater than the static stiffness values, which is also true for the predicted seismic and static values. Thus, the HSVN model here shows its ability to capture the observed differences between the seismic and static stiffnesses. That means the difference between the static and seismic joint stiffnesses was attributed to the dynamical effects concerning the strain rate and strain level. The stiffness data from transducer 8S was similar to that of 2S and therefore not shown here. Transducers 2S and 8S are symmetrically arranged in the experiment (please see Fig. 6). The presentation here only focusses on the behavior as observed by transducers 2S, 4S, and 5S.

Fig. 11 provides a comparison between the model predictions and laboratory measurements of the static and seismic shear stiffnesses for joint specimen J-0.17. Since J-0.17 was rougher than J-0.11, the stress drop after the peak was more significant. The failure process was characterized by asperity shearing instead of frictional slipping. Precursor events also were observed in both the predicted and measured seismic stiffness values. While the stiffness degradation after the precursors was relatively steady for this rougher joint, it experienced a sudden change near the peak stress. The joint static stiffness values, both the predicted and the measured, fluctuated slightly as the shear load was applied to the specimen and then dropped to a very small value near the peak stress. Similar to the specimen J-0.11, the seismic stiffness values were around three to five times greater than the static stiffness values. The observed difference between the seismic and static joint stiffnesses was captured successfully by the HSVN joint model.

Note that the agreement between the predicted and measured values of the static shear stiffness is not good enough in this study. A possible explanation for this mismatch is related to the difference in stress\displacement values adopted in seismic and static calculations. The measured static stiffness was calculated based on the stress corresponding to the entire joint area and the displacement extracted from the lateral surface. In contrast, the predicted stiffness values were calculated by seismic wave propagation, which examined the stress-strain response within a small area determined by the diameter of the ultrasonic transducers. Although the mismatch appeared to be an irreconcilable issue, it is encouraging that the observed difference between the seismic and static joint stiffnesses is captured for the first time by assuming the HSVN model.

Fig. 12 shows the measured and predicted transmission coefficients as a function of frequency at the residual-strength stage for joint specimens J-0.11 and J-0.17. The exact value of η thus was determined by assuming a Maxwell model with η being equal to 5.88 $kPa \cdot s/m$ for specimen J-0.11 and 4.68 $kPa \cdot s/m$ for J-0.17. Good agreement was observed at both the low and high frequencies, indicating that assuming a Maxwell model, i.e., assuming k_1' decreases to zero in the HSVN model, was shown to be a reasonable approach for predicting the wave energy dissipation in the residual-strength phase.

5 Discussion

Although relatively good agreement was achieved between the predicted and the measured spectral amplitudes by assuming the DDM, as shown in Fig. 7b. There were discrepancies consistently at frequencies lower than the dominant frequency, i.e., the predicted spectrum was typically larger than the measured one at the low frequencies. This mismatch has been studied by Pyrak-Nolte &Nolte[22] and Cai[16]. They contended that it was caused by the frequency dependency of joint stiffness, i.e., joint stiffness should be smaller at low frequencies than at high frequencies.

Fig. 13 shows examples of the S-wave spectra predicted by assuming the DDM and the velocity displacement model, i.e., the HSVN model, while providing a comparison with the measured spectrum. A better prediction of the spectrum for the shear wave transmitted across a joint was obtained by assuming the HSVN model. The discrepancy at the frequencies lower than the dominant frequency was very small. A better agreement also was achieved at high frequencies. This improvement was due to the frequency-dependent stiffness property incorporated in the HSVN model. As mentioned earlier, the fixed joint stiffness assumed in the DDM represented the average stiffness in the frequency domain, while the stiffness in the HSVN model was frequency-dependent.

Taking the real part of Eq. (4), the global stiffness of the HSVN model can be rewritten as:

$$k = \sqrt{\frac{k_0^{\,2} k_1^{\,2} + k_0^{\,2} \eta^2 \omega^2}{\left(k_0 + k_1\right)^2 + \eta^2 \omega^2}} \tag{11}$$

Thus, the upper and lower boundary values of the shear stiffness for a HSVN contact can be determined as:

$$k_{(\omega\to\infty)} = k_0 \tag{12}$$

$$k_{(\omega\to 0)} = \frac{k_0 k_1^{'}}{k_0 + k_1^{'}} \tag{13}$$

Fig. 14 compares the joint stiffnesses defined by the HSVN model and the DDM as a function of frequency. Like other velocity displacement models, the HSVN model shows the clear dependence between stiffness and frequency. For high frequencies, the stiffness of the HSVN model gradually approached k_0, which was exactly the small-strain stiffness given by the Hooke element. For low frequencies, the stiffness had a minimum value, i.e., $k_0 k_1'/(k_0+k_1')$, which was the rate-independent stiffness given by the HSV model. Therefore, Eqs. (11-13) literally quantified the stiffness-frequency relationship defined by the HSVN model. The small-strain response characterized the high frequency behavior of the HSVN model, while the rate-independent response characterized the low frequency behavior. For this reason, the observed difference between the seismic and static joint stiffnesses can be captured by the HSVN model.

5 Conclusions

In this study, a velocity discontinuity model composed of Hooke, modified Saint Venant, and Newton elements was developed to interpret the experimentally collected shear wave transmitted through a rock joint. The small-strain stiffness defined by the model is relevant to the wave energy dissipation at high frequencies, providing an approximate value of joint seismic stiffness. The rate-independent stiffness of this model is associated with joint deformation at low frequencies, providing an estimation of the static stiffness. Compared to the DDM, the developed joint model has the capacity to describe the stiffness variation in the frequency domain. Therefore, a better prediction of spectra for shear waves transmitted across a joint is achieved, and the observed difference between the seismic and static joint stiffnesses is successfully captured. Moreover, dynamic effects on shear behaviour of joints is related to strain rate and strain level, which are at the core of the concept on the frequency-dependent joint stiffness.

Acknowledgements

We would like to give our special thanks to Prof. Jianbo Zhu from Shenzhen University for his unique viewpoints on rate effects. This manuscript was funded by the NSFC (Nos.: 42102320 and U19A2098), and by the attachment programme from the Hong Kong Polytechnic University.

References

[1] Barton N, Bandis S, Bakhtar K. Strength, deformation and conductivity coupling of rock joints. Int. J. Rock Mech. Min. Sci. Geomech. Abstr. 1985; 22(3): 121-140.

[2] Ma GW, Li JC, Zhao J. Three-phase medium model for filled rock joint and interaction with stress waves. Int. J. Numer. Anal. Methods Geomech. 2010; 35(1): 97-110.

[3] Wu W, Li JC, Zhao J. Loading Rate Dependency of Dynamic Responses of Rock Joints at Low Loading Rate. Rock Mech. Rock Eng. 2012; 45(3): 421-426.

[4] Goodman RE. Methods of geological engineering in discontinuous rocks. New York, USA: West Publishing; 1976.

[5] Petrovitch CL, Pyrak-Nolte LJ, Nolte DD. Combined Scaling of Fluid Flow and Seismic Stiffness in Single Fractures. Rock Mech. Rock Eng. 2014; 47(5): 1613-1623.

[6] Pyrak-Nolte LJ, Morris J. Single fractures under normal stress: The relation between fracture specific stiffness and fluid flow. Int. J. Rock Mech. Min. Sci. 2000; 37: 245-262.

[7] Zhang QB, Zhao J. A review of dynamic experimental techniques and mechanical behaviour of rock materials. Rock Mech. Rock Eng. 2014; 47(4): 1411-1478.

[8] Gu B, Suárez-Rivera R, Nihei KT, Myer LR. Incidence of plane waves upon a fracture. J. Geophys. Res.-Solid Earth. 1996; 101(B11): 25337-25346.

[9] Choi MK, Bobet A, Pyrak-Nolte LJ. The effect of surface roughness and mixed-mode loading on the stiffness ratio κx/κz for fractures. Geophysics. 2014; 79(5): D319-D331.

[10] Pyrak-Nolte LJ, Myer LR, Cook NGW. Anisotropy in seismic velocities and amplitudes from multiple parallel fractures. J. Geophys. Res.-Solid Earth. 1990; 95(B7): 11345-11358.

[11] Atkinson JH. Non-linear soil stiffness in routine design. Géotechnique. 2000; 50(5): 487-508.

[12] Hencher SR, Friction parameters for the design of rock slopes to withstand earthquake loading. In: Dams and Earthquake. Thomas Telford Publishing; 1981. pp. 74-89.

[13] Kana DD, Fox DJ, Hsiung SM. Interlock/friction model for dynamic shear response in natural jointed rock. Int. J. Rock Mech. Min. Sci. Geomech. Abstr. 1996; 33(4): 371-386.

[14] Cui Z, Sheng Q, Leng X, Ma Y. Analysis of the seismic performance of a rock joint with a modified continuously yielding model. Rock Mech. Rock Eng. 2017; 50(10): 2695-2707.

[15] Barton N, Some aspects of rock joint behaviour under dynamic conditions. In: Mechanics and Engineering of Rocks. Torino Politecnica; 1988. pp.71-82.

[16] Cai JG, Effects of parallel fractures on wave attenuation in rock. PhD thesis. Nanyang Technological University, Singapore; 2001.

[17] Cai M, Kaiser PK, Suorineni F, Su K. A study on the dynamic behavior of the Meuse/Haute-Marne argillite. Phys. Chem. Earth, Parts A/B/C. 2007; 32(8): 907-916.

[18] Zhao J, Cai JG, Zhao XB, Li HB. Experimental study of ultrasonic wave attenuation across parallel fractures. Geomech. Geoeng. 2006; 1(2): 87-103.

[19] Benedetto DH, Tatsuoka F. Small strain behavior of geomaterials: modelling of strain rate effects. Soils Found. 1997; 37(2): 127-138.

[20] Cha M, Santamarina JC, Kim H, Cho G. Small-Strain Stiffness, Shear-Wave Velocity, and Soil Compressibility. J. Geotech. Geoenviron. Eng. 2014; 140(10): 06014011.

[21] Królikowski J, Szczepek J. Assessment of tangential and normal stiffness of contact between rough surfaces using ultrasonic method. Wear. 1993; 160(2): 253-258.
[22] Pyrak-Nolte LJ, Nolte DD. Frequency dependence of fracture stiffness. Geophys. Res. Lett. 1992; 19(3): 325-328.
[23] Zhu JB, Perino A, Zhao GF, Barla G, Li JC, Ma GW, Zhao J. Seismic response of a single and a set of filled joints of viscoelastic deformational behaviour. Geophys. J. Int. 2011; 186(3): 1315-1330.
[24] Zhu JB, Zhao XB, Wu W, Zhao J. Wave propagation across rock joints filled with viscoelastic medium using modified recursive method. J. Appl. Geophys. 2012; 86: 82-87.
[25] Pyrak-Nolte LJ, Myer LR, Cook NGW. Transmission of seismic waves across single natural fractures. J. Geophys. Res.-Solid Earth. 1990; 95(B6): 8617-8638.
[26] Kendall K, Tabor D. An utrasonic study of the area of contact between stationary and sliding surfaces. Proc. R. Soc. London Ser. A-Math. Phys. Eng. Sci. 1971; 323(1554): 321-340.
[27] Myer L, Hopkins D, Cook N. Effects of contact area of an interface on acoustic wave transmission characteristics. In: 26th U.S. Rock Mechanics Symposium. Boston, 1985. p. 565-572.
[28] Królikowski J, Szczepek J, Witczak Z. Ultrasonic investigation of contact between solids under high hydrostatic pressure. Ultrasonics. 1989; 27(1): 45-49.
[29] Pyrak-Nolte LJ. The seismic response of fractures and the interrelations among fracture properties. Int. J. Rock Mech. Min. Sci. Geomech. Abstr. 1996; 33(8): 787-802.
[30] Li J, Ma G, Zhao J. Stress wave interaction with a nonlinear and slippery rock joint. Int. J. Rock Mech. Min. Sci. 2011; 48(3): 493-500.
[31] Zhu JB, Li H, Deng JH. A one-dimensional elastoplastic model for capturing the nonlinear shear behaviour of joints with triangular asperities based on direct shear tests. Rock Mech. Rock Eng. 2019; 52: 1671–1687
[32] Sigenori K, Azuhiko S, Minoru K. On the mechanical behaviour of rocks under impulsive loading. Bull. Fac. Eng., Hokkaido Univ. 1977; 83: 51-62.
[33] Mutlu O, Bobet A. Slip initiation on frictional fractures. Eng. Fract. Mech. 2005; 72(5): 729-747.
[34] Comninou M, Barber JR, Dundurs J. Interface slip caused by a surface load moving at constant speed. Int. J. Mech. Sci. 1983; 25(1): 41-46.
[35] Malanchuk N, Martynyak R. Contact interaction of two solids with surface groove under proportional loading. Int. J. Solids Struct. 2012; 49(23): 3422-3431.
[36] Mutlu O, Bobet A. Slip propagation along frictional discontinuities. Int. J. Rock Mech. Min. Sci. 2006; 43(6): 860-876.
[37] Sibson RH. Earthquake faulting as a structural process. J. Struct. Geol. 1989; 11(1): 1-14.
[38] Elsworth D, Spiers CJ, Niemeijer AR. Understanding induced seismicity. Science. 2016; 354(6318): 1380-1381.
[39] Pan B, Qian K, Xie H, Asundi A. Two-dimensional digital image correlation for in-plane displacement and strain measurement: a review. Meas. Sci. Technol. 2009; 20(6): 062001.
[40] Hedayat A, Pyrak-Nolte LJ, Bobet A. Multi-Modal Monitoring of Slip Along Frictional Discontinuities. Rock Mech Rock Eng. 2014; 47(5): 1575-1587.
[41] Hedayat A, Pyrak-Nolte LJ, Bobet A. Detection and Quantification of Slip Along Non-Uniform Frictional Discontinuities Using Digital Image Correlation. ASTM Geotech. Test. J. 2014; 37(5): 786-799.
[42] Królikowski J, Szczepek J. Prediction of contact parameters using ultrasonic method. Wear. 1991; 148(1): 181-195.
[43] Hedayat A, Pyrak-Nolte LJ, Bobet A. Precursors to the shear failure of rock discontinuities. Geophys Res Lett. 2014; 41(15): 5467-5475.

[44] Li H, Zhou T, Deng J, Yin J, Zhu J. An excess stress model for capturing rate-dependent compressive behavior of rock joint and its validation and applications. Int. J. Rock Mech. Min. Sci. 2020; 128: 104267.
[45] Li H, Deng J, Yin J, Qi S, Zheng B, Zhu J. An experimental and analytical study of rate-dependent shear behaviour of rough joints. Int. J. Rock Mech. Min. Sci. 2021; 142: 104702.
[46] Zhou ZL, Cai X, Zhao Y, Chen L, Xiong C, Li XB. Strength characteristics of dry and saturated rock at different strain rates. Trans. Nonferrous Met. Soc. China. 2016; 26(7): 1919-1925.
[47] Hedayat A, Walton G. Laboratory determination of rock fracture shear stiffness using seismic wave propagation and digital image correlation. Geotech. Test. J. 2017; 40(1): 92-106.
[48] Gheibi A, Hedayat A. Ultrasonic investigation of granular materials subjected to compression and crushing. Ultrasonics. 2018; 87: 112-125.
[49] Patel S, Martin C. Application of Digital Image Correlation Technique for Measurement of Tensile Elastic Constants in Brazilian Tests on a Bi-Modular Crystalline Rock. Geotech. Test. J. 2018; 41(4): 664-674.
[50] Shirole D, Walton G, Hedayat A. Experimental investigation of multi-scale strain-field heterogeneity in rocks. Int. J. Rock Mech. Min. Sci. 2020; 127: 104212.
[51] Hedayat A, Haeri H, Hinton J, Masoumi H, Spagnoli G. Geophysical Signatures of Shear-Induced Damage and Frictional Processes on Rock Joints. J. Geophys. Res.-Solid Earth. 2018; 123(2): 1143-1160.
[52] Snieder R, Grêt A, Douma H, Scales J. Coda Wave Interferometry for Estimating Nonlinear Behavior in Seismic Velocity. Science. 2002; 295(5563): 2253.

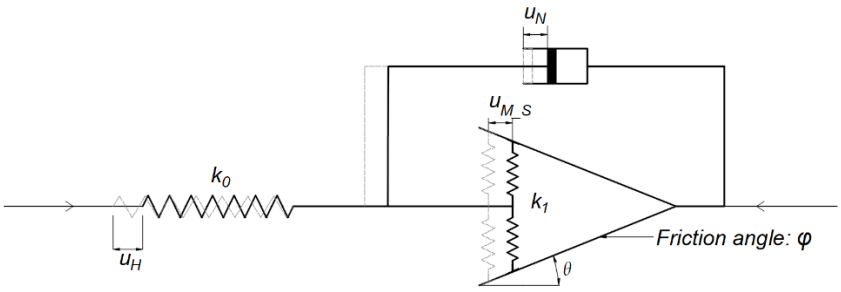

Fig. 1 Sketch of the Hooke-modified Saint Venant/Newton (HSVN) model[44]. k_0 and k_1 are spring stiffnesses; u_H, u_{M_S} and u_N are the respective displacements of the three elements; θ and φ are the dip angle and fictional angle of frictional surfaces in the modified Saint Venant element.

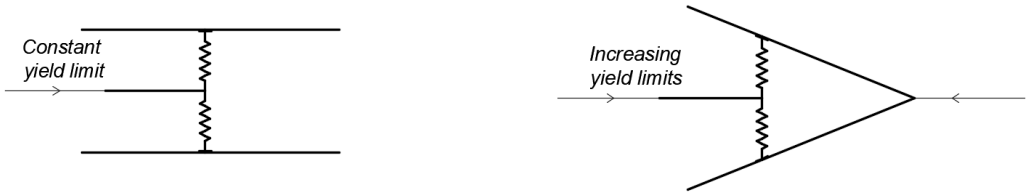

(a) (b)

Fig. 2 Sketches of the (a) traditional and (b) modified Saint Venant elements (adapted after Zhu *et al.*[31]).

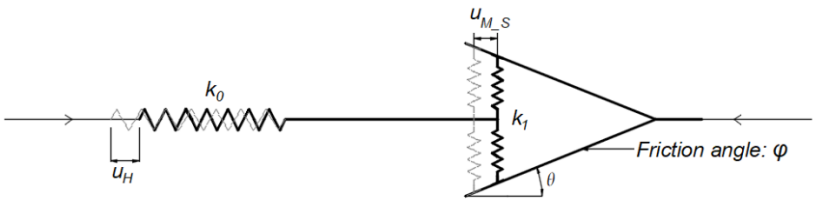

Fig. 3 Sketch of the Hooke-modified Saint Venant (HSV) model (adapted after Zhu *et al.*[31]).

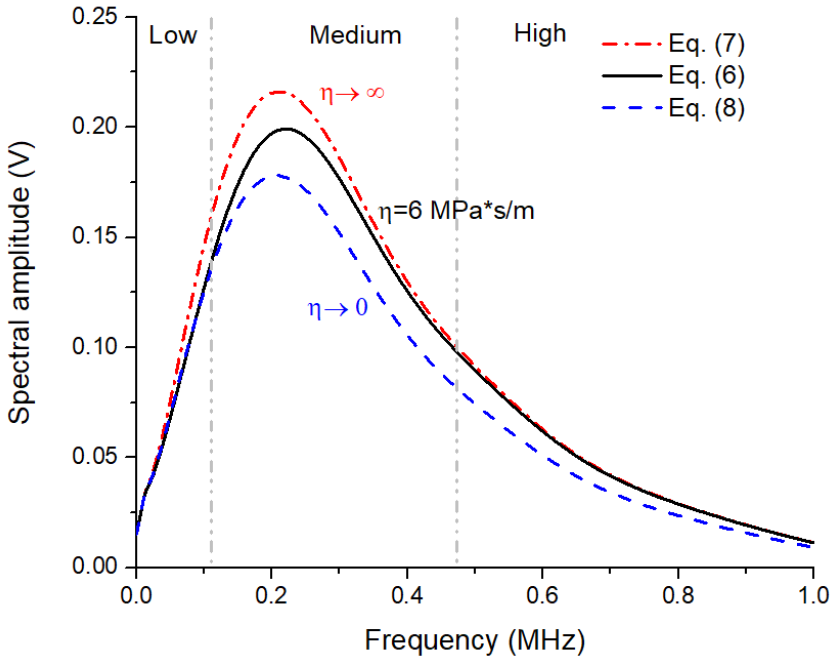

Fig. 4 Comparison of the S-wave spectra calculated by **Eqs. (6), (7) and (8).** Waveform data were collected by the transducer 5S in the direct shear test of the joint specimen J-0.11 at time 700 s.

(a) (b) (c)

Fig. 5 Images of (a) a grooved sandstone block, (b) the textured spray paint on the outward-facing surface as well as (c) the obtained joint surfaces and roughness measurement (joint specimens were labelled as "J-Z_2".)

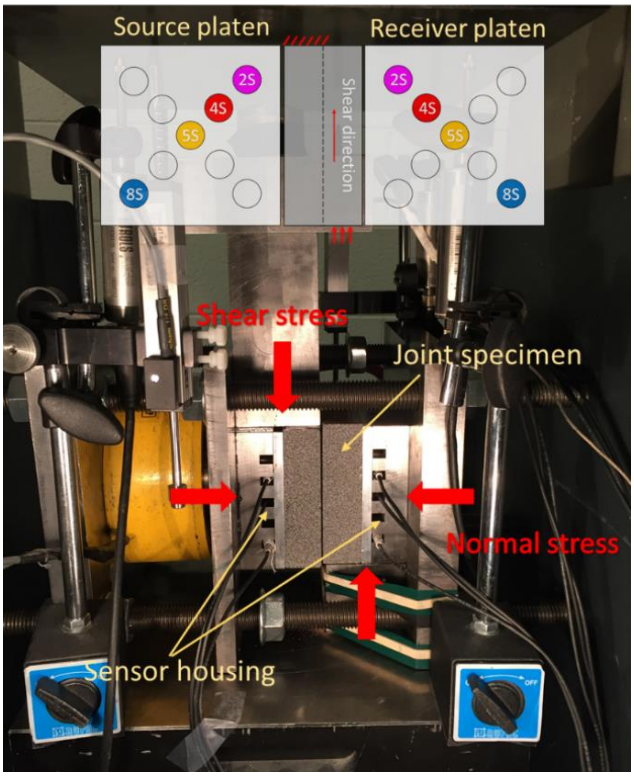

Fig. 6 The direct shear apparatus with embedded S-wave transducers. (Inset: Transducer layout for seismic measurements; 2S, 4S, 5S and 8S denote S-wave transducers at different locations)

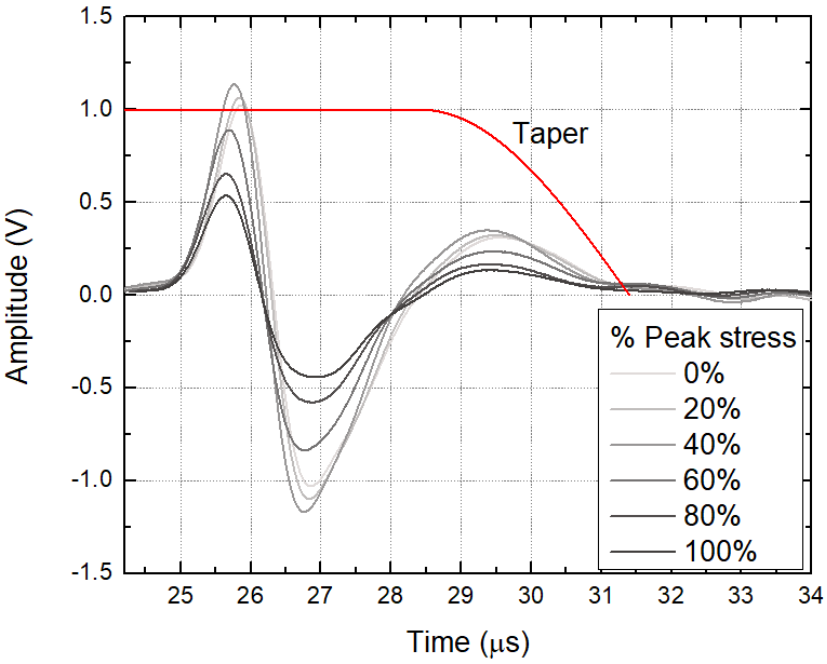

(a)

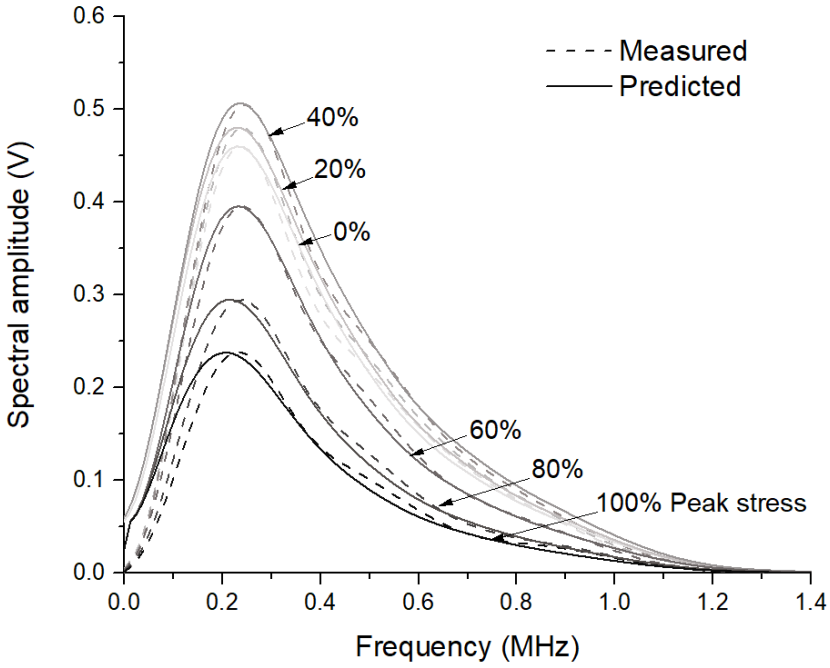

(b)

Fig. 7 Determination of seismic joint stiffness by spectral analysis: (a) the transmitted shear waveforms recorded during shearing and the taper used to compute the spectral content; (b) the measured S-wave spectra and the predicted ones based on the DDM. Waveform data were collected by the transducer 2S in the direct shear test of the joint specimen J-0.11.

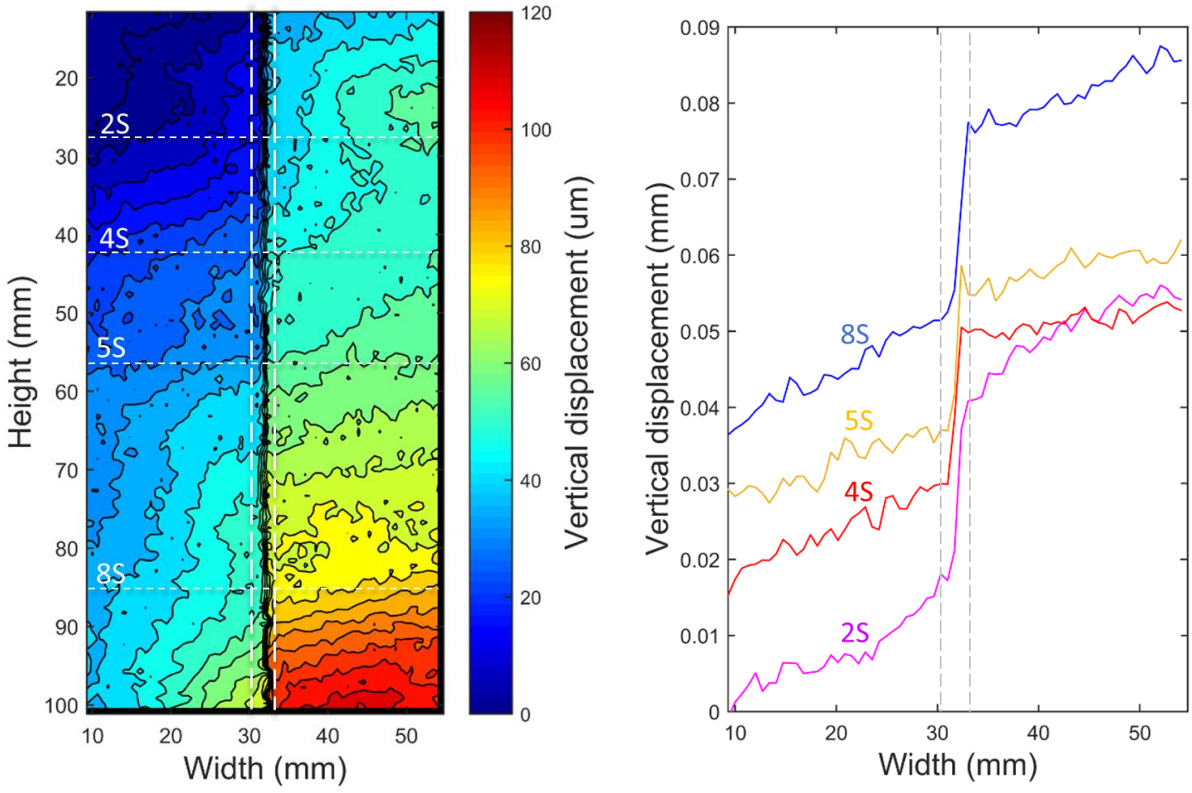

(a) (b)

Fig. 8 Relative shear displacement measured by DIC: (a) vertical/shear displacement contour at the moment of shear failure and (b) relative vertical/shear displacement profiles at four cross sections showing the projected center of the ultrasonic transducers. Data comes from the direct shear test of the joint specimen J-0.11.

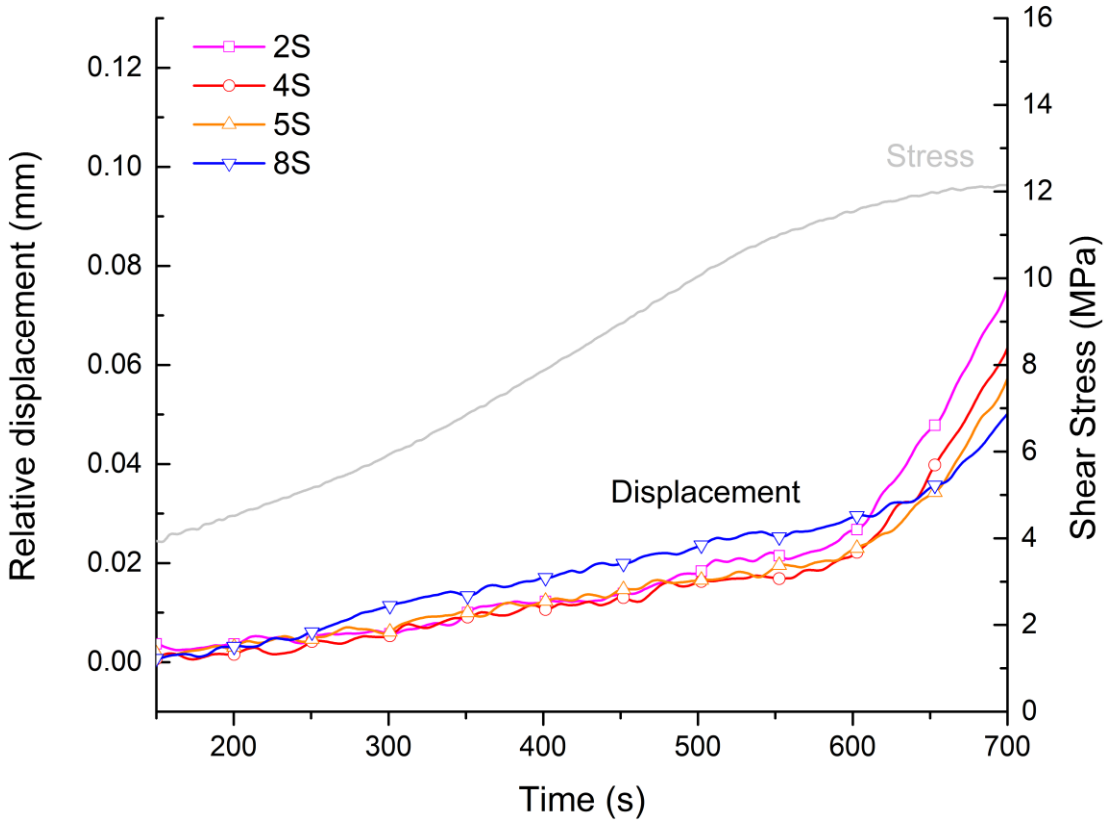

Fig. 9 The shear stress and the measured relative shear displacements at four cross sections as a function of time measured from the direct shear test of the joint specimen J-0.11.

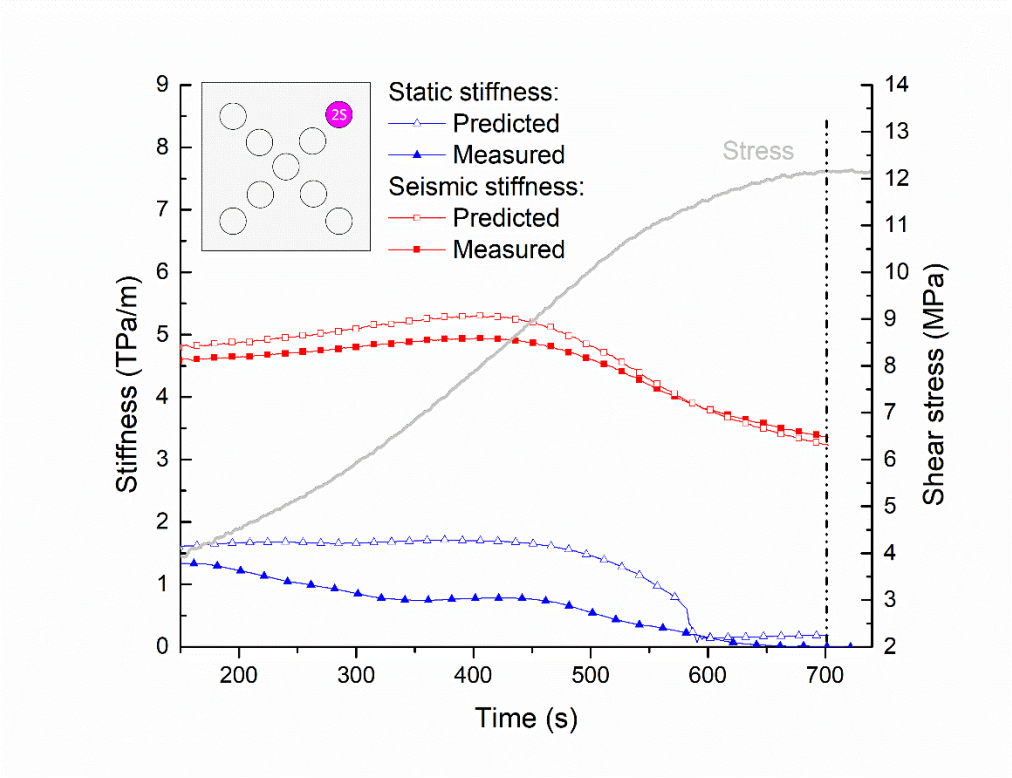
2S
Static stiffness:
Predicted
Measured
Seismic stiffness:
Predicted
Measured
Stress
Stiffness (TPa/m)
Shear stress (MPa)
Time (s)

(a)

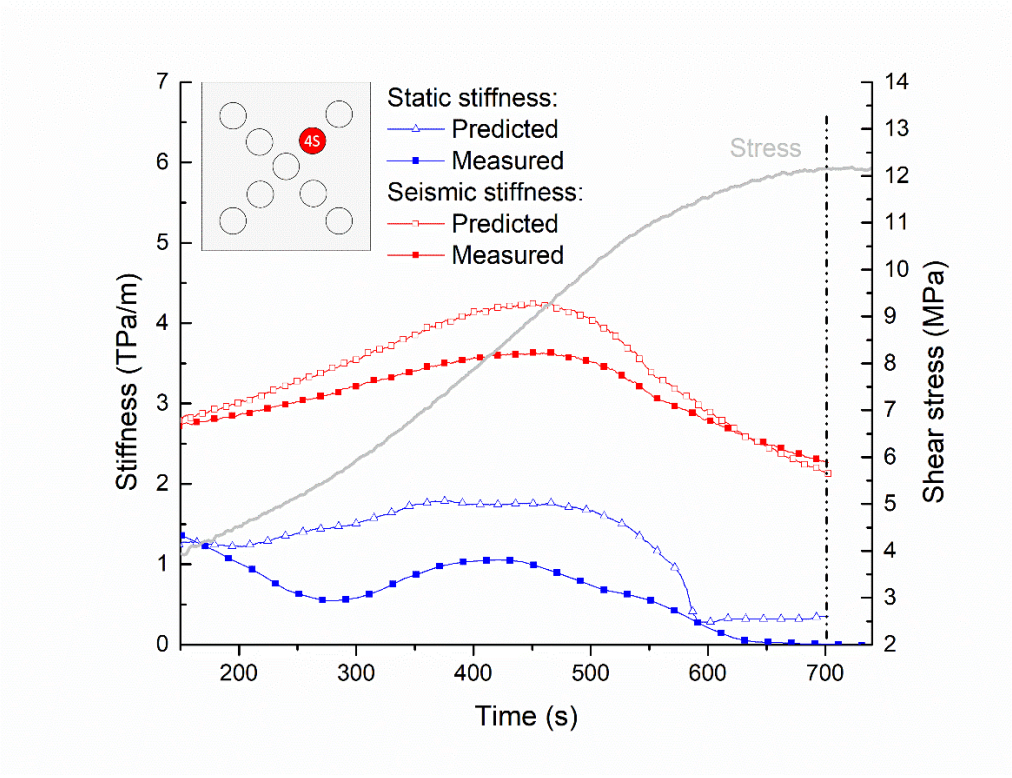
4S
Static stiffness:
Predicted
Measured
Seismic stiffness:
Predicted
Measured
Stress
Stiffness (TPa/m)
Shear stress (MPa)
Time (s)

(b)

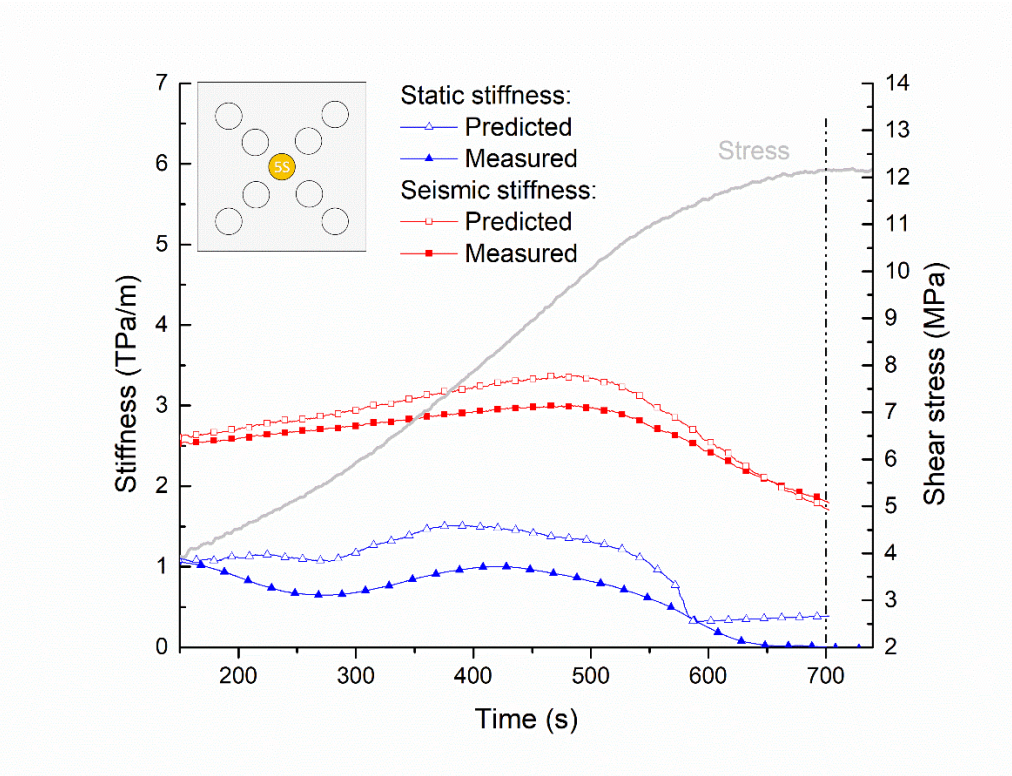

(c)

Fig. 10 Variations of the shear stress, the static and seismic shear stiffnesses during shearing for the joint specimen J-0.11. The measured static stiffness was obtained based on the DIC technique, and the measured seismic stiffness was calculated by assuming the DDM. The predicted static and seismic stiffnesses were both determined by assuming the HSVN model. The dash line indicates the time corresponding to the peak stress.

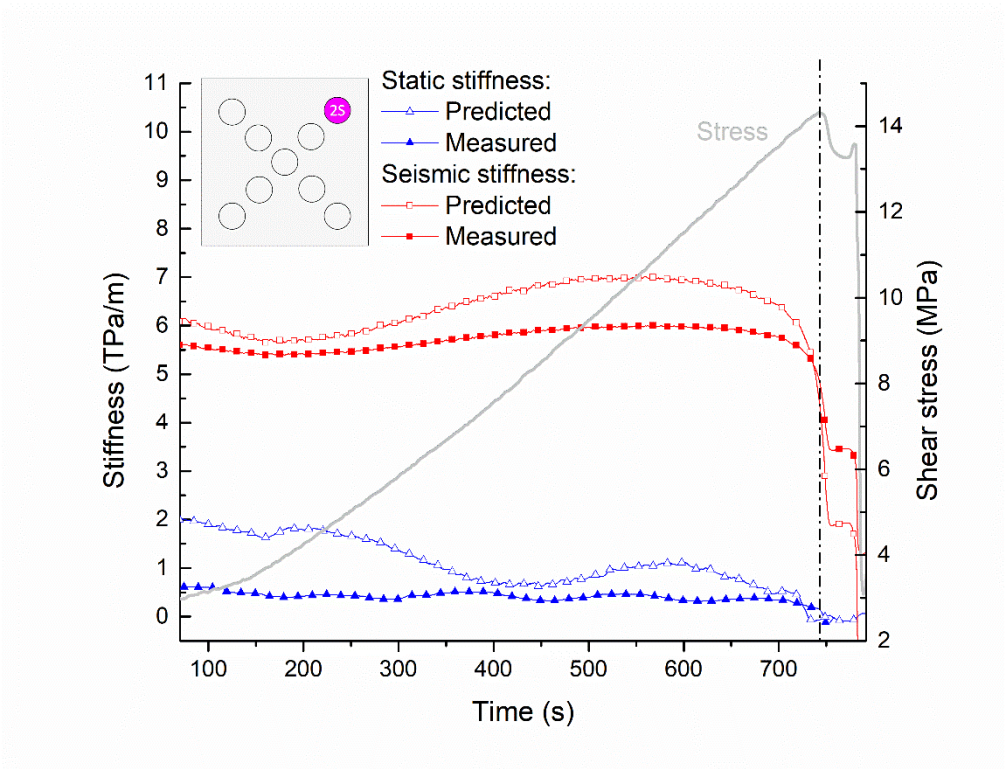
Static stiffness:
Predicted
Measured
Seismic stiffness:
Predicted
Measured
Stress
2S
Stiffness (TPa/m)
Shear stress (MPa)
Time (s)

(a)

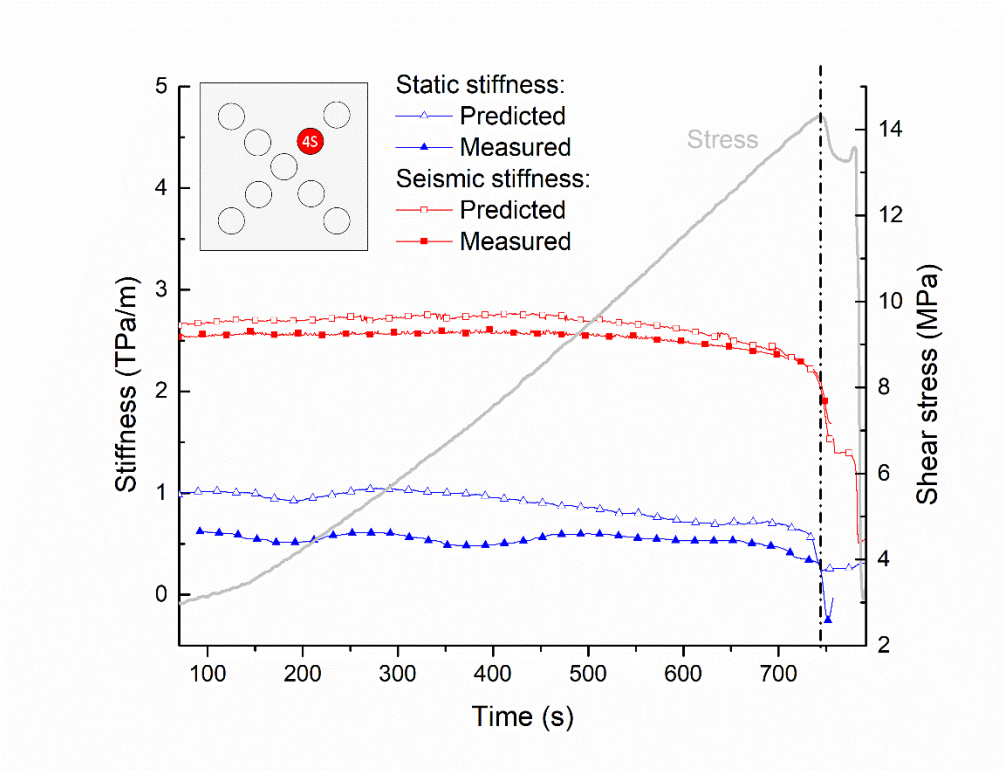
Static stiffness:
Predicted
Measured
Seismic stiffness:
Predicted
Measured
Stress
4S
Stiffness (TPa/m)
Shear stress (MPa)
Time (s)

(b)

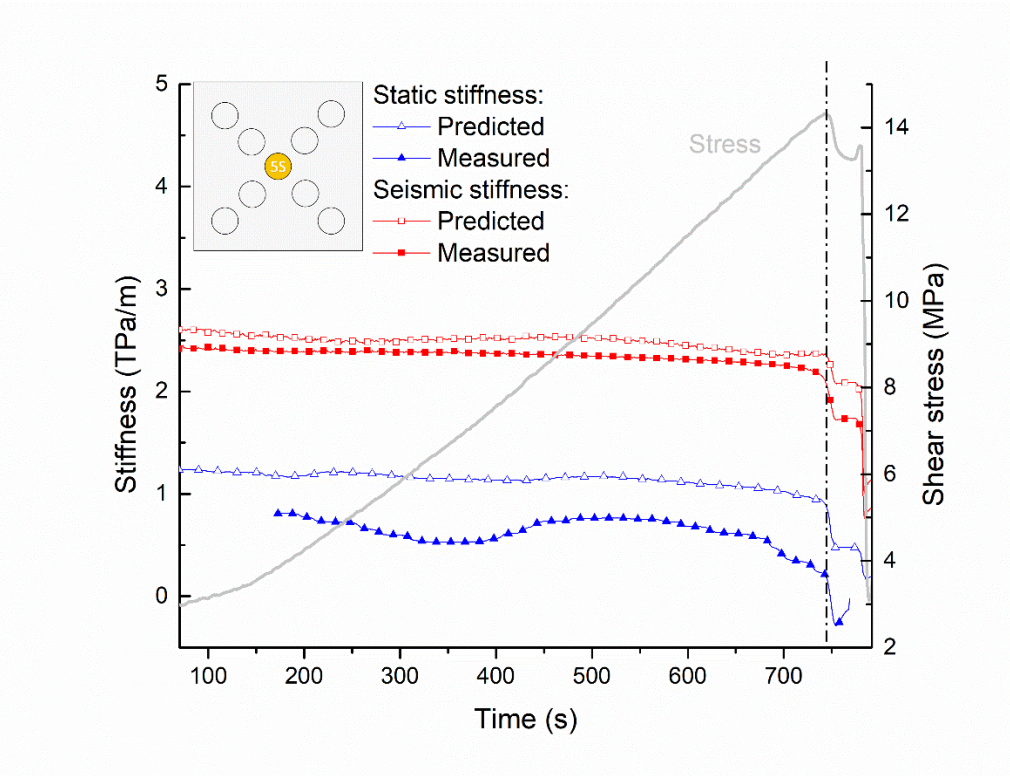

(c)

Fig. 11 Shear stress-time curves and static and seismic shear stiffnesses for joint specimen J-0.17. The measured static stiffness was obtained based on the DIC technique, and the measured seismic stiffness was calculated by assuming the DDM. The predicted static and seismic stiffnesses were both determined by assuming the HSVN model. The dash line indicates the time corresponding to the peak stress.

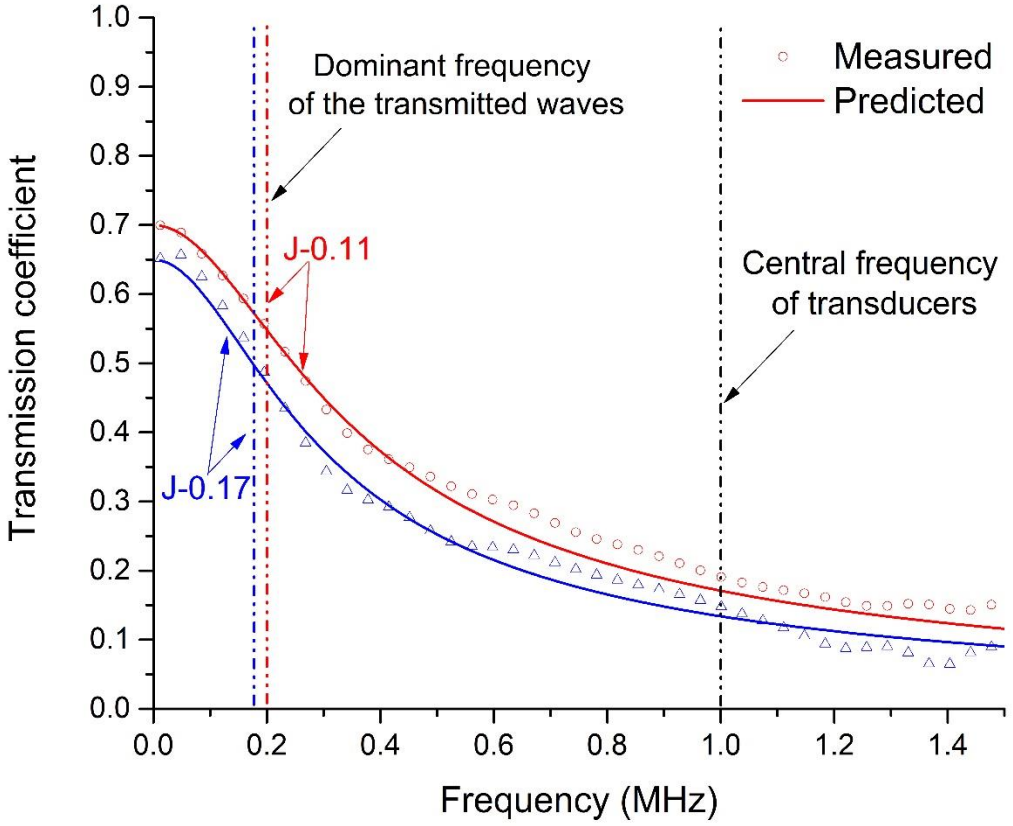

Fig. 12 The measured and the predicted transmission coefficients as a function of frequency at the residual-strength stage of the joint specimens J-0.11 and J-0.17.

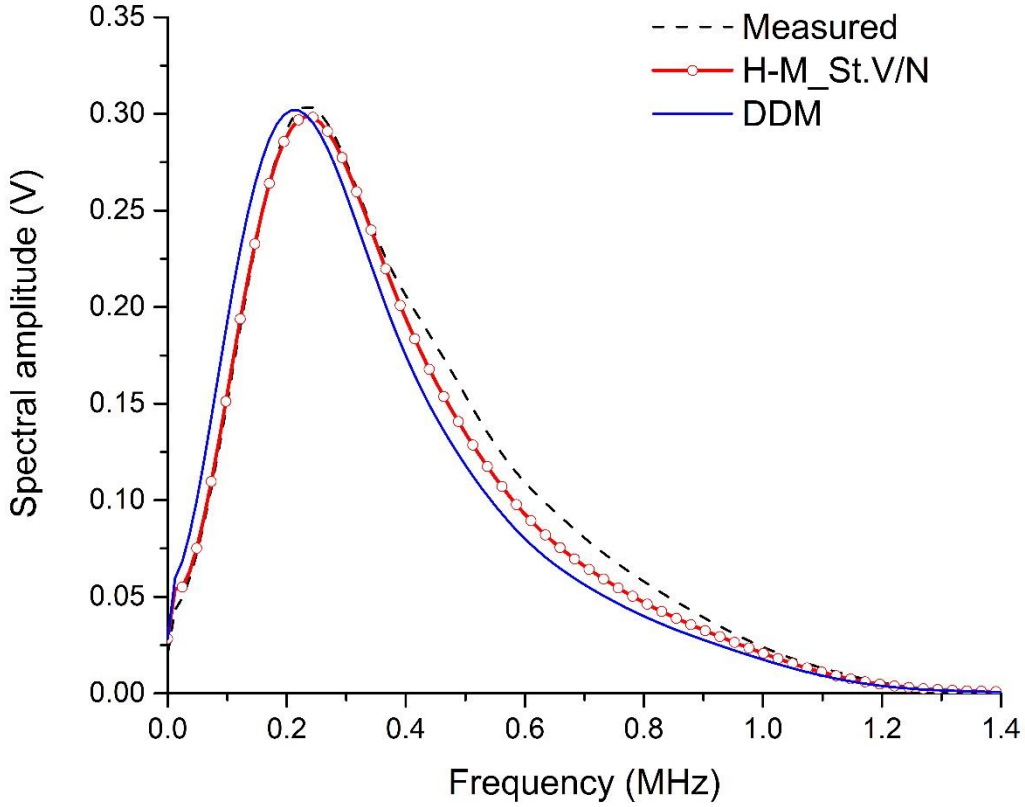

Fig. 13 Comparison of S-wave spectra predicted by assuming the HSVN model and the DDM. Waveform data were collected by the transducer 4S in the shear test of the joint specimen J-0.11 at time 700 s.

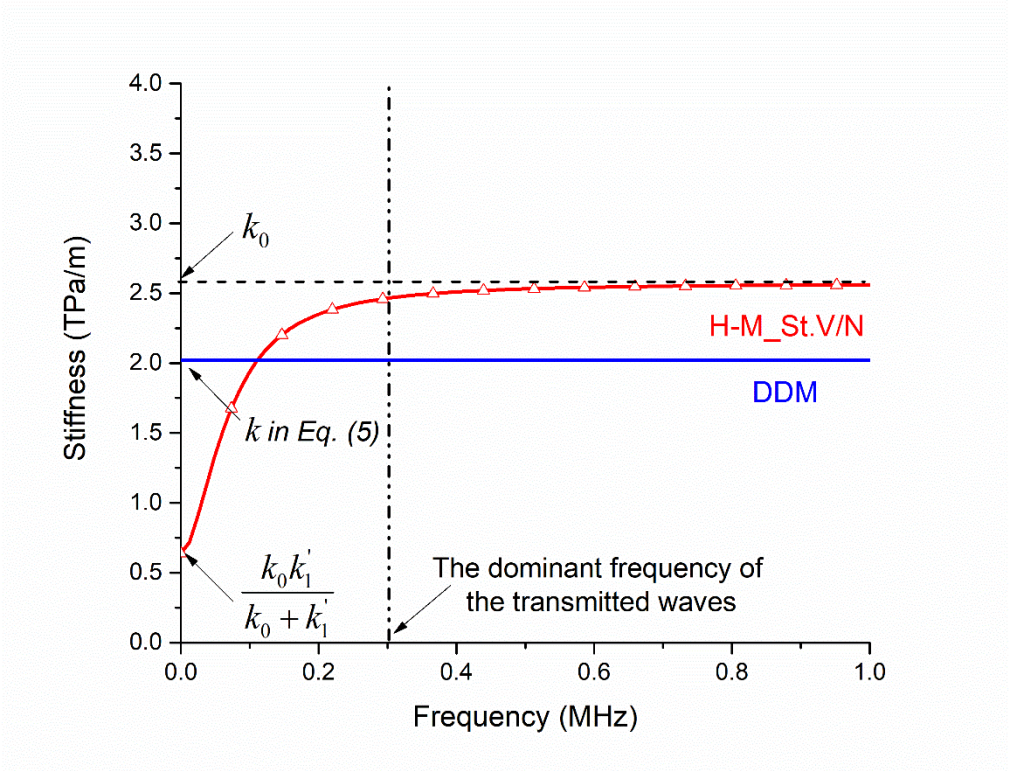

Fig. 14 The stiffness-frequency relationship defined by the HSVN model and the DDM. The stiffness values were calculated based on the same wave-form data collected by the transducer 5S in the direct shear test of the joint specimen J-0.07 at time 100 s.

Table 1 Physical and mechanical properties of the sandstone material

Properties	**values**
Density (g/cm^3)	2.33
Uniaxial compressive strength (MPa)	69.70
Young's modulus (GPa)	15.65
Poisson's ratio	0.21
Shear-wave velocity (m/s)	2208.58